Rev. Roum. Sci. Techn.– Électrotechn. et Énerg.
Vol. **67**, *3*, pp. 321–326, Bucarest, 2022

CIRCULAR POLARIZED TWO-ELEMENT COMPACT DUAL-BAND MIMO ANTENNA FOR 5G AND WEARABLE APPLICATIONS

PRAGYA GUPTA [1], MANISHA BHARTI [1], ANUBHAV KUMAR [2]

Keywords: Multiple input multiple output antenna; Circular polarization; 5G; Specific absorption rate; Wearable and cancer detection applications.

In this paper, a compact dual-band circular polarization (CP) multiple input multiple output (MIMO) antenna is proposed that can be used for 5G and wearable applications. The proposed antenna comprises two rectangular radiators used to obtain the dual-band response. The defected ground approach is used to mitigate the effect of surface current between the ports. Two open-ended stubs with T-shaped decoupling are used to improve the isolation between the ports without affecting the antenna parameters and the radiation pattern. The distance between two radiators is 0.31 λ_0 which causes the high mutual coupling between the antennas. The two symmetric open-ended stubs are introduced to improve the isolation up to 17 dB at higher operating frequencies and are responsible for circular behavior. A T-shaped stub is inserted in the ground that improves the isolation up to 10 dB at a lower frequency. The dual-band response of the proposed antenna is observed from 3.0 GHz to 3.6 GHz covers 5G (n78) and 5.7 GHz to 9.7 GHz, which covers direct sequence (DS) ultra-wideband (UWB), smartphone, wearable, and biomedical applications. The proposed antenna shows circular behavior in the ISM band therefore, the proposed SAR is simulated and analyzed for wearable and cancer detection applications.

1. INTRODUCTION

In the recent era of modern communication systems, 5G is the emerging technology that demands a high data rate, minimum delay, and large channel capacity. Single input single output (SISO) system [1] cannot satisfy all these needs therefore, the present scenario requirements can be resolved by adopting the multiple-input multiple-output (MIMO) technology that can provide a high data rate with minimum multipath interference, high channel capacity, low latency, better link reliability, and higher spectral efficiency. MIMO antenna utilizes multiple antennas at the receiver and transmitter side to transmit multiple signals simultaneously over the same channel. According to the requirement of the recent technology, the antenna size should be compact so that it can be accomplished with portable and wearable devices. When the MIMO antennas are integrated with electronic devices in a compact space, the mutual coupling between the antenna elements increases, affecting the MIMO antenna parameters. To eliminate the coupling effect between the MIMO antenna elements in a compact size, decoupling technology is used in literature with dual-band characteristics [1–10]. The antennas in literature for decoupling technology (transmission line decoupling network [2], meandering lines [3, 4, 9], metal strip with shorting vias [5], metamaterial [6], parasitic stubs [7,8], WG-MTM [9], stubs connected with ground [10]) increases the size of an antenna and simultaneously decoupling technology is complex which could be impractical for wearable and portable applications. In the literature, the incorporation of decoupling technology such as meandering line and parasitic elements [4], slots and floating stubs [7], unconnected metal strips [8], and meandering line and slot [11] between antenna elements influence the operating bandwidth and resonance frequency of an antenna that affect the practical application of antenna.

In [12], dual-band is achieved by a two-port inverted F-shaped antenna, and three T-stubs are used to reduce the mutual coupling. Therefore, considering practical applications, effective decoupling technology is proposed to reduce the mutual coupling without affecting the operating bandwidth and resonant frequency of the antenna. Simultaneously the antenna exhibits circularly polarized behavior in which the strength of the received signal is constant irrespective of antenna orientation, thereby performing better than a linear polarized antenna [13]. Telemedicine [14], and machine learning [15] in the biomedical and electromagnetic wave are used to improve the quality of life where compact MIMO antenna can be beneficial for wearable and biomedical applications.

In the CP antenna, all the power is divided equally into all the receiving radiators, and signals are received with the same intensity irrespective of the antenna's orientation compared to LP radiators [16]. MIMO with circular polarization is also discussed in reference [13,17], whereas very few works are published in the literature to achieve CP characteristics in dual-band MIMO antenna.

According to the requirement of portable and wearable devices in recent technology, a compact CP dual-band two-port antenna with an easy decoupling structure is used to enhance the isolation for 5G (n78) and ISM/WLAN applications.

The technical contributions to the novelty of the proposed antenna are as follows:

- A CP radiator in a MIMO antenna provides better power channel gain and channel capacity loss than LP radiators in LOS and multi-path environments where the MIMO antenna is not perfectly aligned [13].
- The T-shaped stub and open-ended slot decoupling structure effectively improve the isolation of the antenna as well as responsible for circular polarization.
- Defected ground decoupling in the proposed antenna is not affecting the resonance frequency of the MIMO antenna, and minimum variation is found. In contrast, more than 20 dB isolation is achieved in operating bandwidth.
- The designed structure is simple and fabricated on low-

[1] National Institute of Technology, Delhi, India, PINCODE-110040; E-mail: pragyagupta@nitdelhi.ac.in
[2] Department of Electronics and Communication, 2 Raj Kumar Goel Institute of Technology & Management, Ghaziabad (UP), India, PINCODE 201003

cost FR4 material that can be easily integrated into portable and wearable devices with minimal effect.

- Antenna design provides a low-loading effect on the human body by minimum variation in antenna parameters.

2. PROPOSED GEOMETRY OF MIMO ANTENNA

The structure of the proposed MIMO antenna is depicted in Fig. 1a, and the hardware prototype is represented in Fig. 1b.

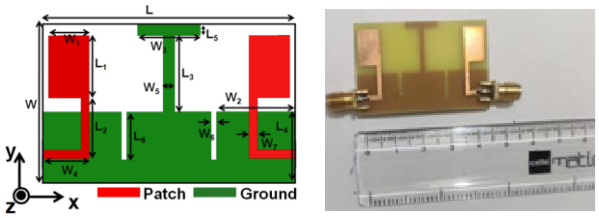

a) b)

Fig. 1 – Proposed antenna: a) dimensions; b) hardware.

The antenna is printed on an FR4 substrate with a dielectric constant of 4.4, a thickness of 0.8 mm (t), and a size of 45 mm × 28 mm.

Parametric variations of the MIMO antenna is illustrated in Fig. 1a, and the values (mm) are as follows: $W = 28$, $L = 45$, $L_1 = 11$, $L_2 = 10.75$, $L_3 = 13.5$, $L_4 = 12.5$, $L_5 = 2$, $L_6 = 8.5$, $W_1 = 7.25$, $W_2 = 14$, $W_3 = 11.2$, $W_4 = 8.25$, $W_5 = 2$, $W_6 = 1$, $W_7 = 1.5 = W_f$.

The design evolution of the two-port antenna is illustrated in four steps and represented in Fig. 2a. In contrast, its corresponding S-parameters and the axial ratio are discussed in Fig. 2b and Fig. 2c, respectively.

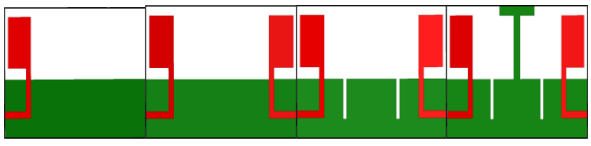

a)

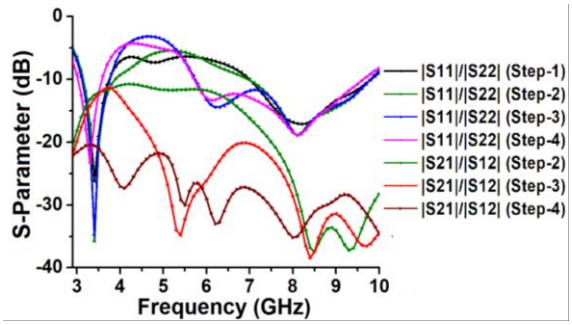

b)

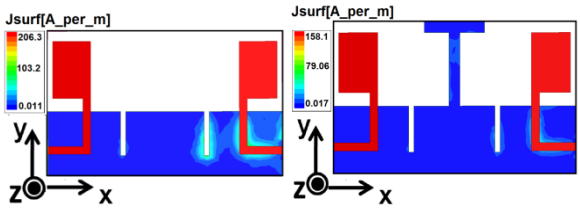

c)

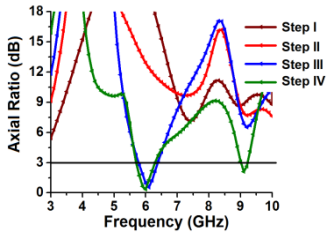

d)

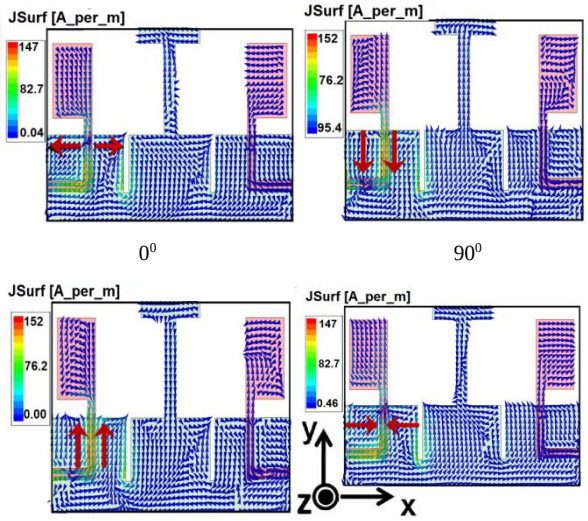

0^0 90^0

180^0 270^0

e)

Fig. 2 – Proposed MIMO antenna evolution: a) design steps; b) simulated S-parameter; c) current distribution at (i) 5.4 GHz (Ant III) (ii) 4.1 GHz (Ant IV); d) axial ratio; e) current distribution at 6 GHz at phase 00, 900, 1 800, 2 700.

The stepwise explanation of the design is as follows:

Step I. The basic structure of the first step is illustrated in Fig. 2a as Antenna-I. The planer rectangular-shaped monopole antenna inspired by half-cutting technology is used with the partial ground, whereas an *L*-shaped microstrip line with 1.5 mm width achieves 50 Ω impedance. The 10 dB impedance bandwidth varies from 3.1 GHz to 3.7 GHz and 7 GHz to 9.8 GHz.

Step II. In the second step, a symmetric and mirror monopole radiator is accomplished, as depicted in Fig. 2a (Antenna-II). The |S11| parameter does not change as in step 1, whereas in this step, high mutual coupling between the antenna elements is achieved where the isolation between port-1 and port-2 is 11 dB.

Step III. To enhance the isolation and impedance matching of the antenna, two open-ended slots are incorporated into the ground plane that changes the current distribution in the ground plane, as shown in the third step of Fig. 2a (Antenna-III). The slot has a length of about $\lambda_0/4$ at the higher resonance frequency. It forces the current to concentrate mainly near it and extends the distance between two ports by enhancing the current path and introducing circular polarization in the higher frequency band. The simulated scattering parameter shows that the bandwidth and isolation of Antenna-III are improved. About 17 dB isolation enhancements are achieved with a symmetrical open stub which perturbs the surface current and reduces the surface wave between the antennas at 8.1 GHz. The isolation in this step is improved and has a higher frequency band from 5.7 GHz to 9.7 GHz, whereas in step IV, isolation is enhanced for a lower frequency.

Step IV. In this step, T-stub is incorporated into the ground between two symmetric open slots, as shown in Fig. 2a (Antenna-IV). It improves the ground in such a way that changes the current movement between the antenna elements by improving the isolation and axial ratio bandwidth. The T-stub enhances the isolation up to 10 dB without affecting the antenna's bandwidth, which ensures an effective decoupling methodology is appropriate for the diverse environment and practical applications.

3. ANALYSIS OF SURFACE CURRENT AND CIRCULAR POLARIZATION

For the better realization of the antenna configuration, the surface current of the simulated states of the MIMO antenna (Antenna-III & Antenna-IV) are demonstrated to reveal the effect of open slots and T-shaped decoupling structure at the frequency 4.1 GHz and 5.4 GHz, respectively in Fig. 2c. The two ports consist of symmetry therefore, the current distribution is demonstrated by exciting port-1. The surface current distribution shows that introduced slots in the ground plane concentrate the current around it and reduce the coupling current to flow from port-1 to port-2. Further, the introduction of a T-shaped decoupling structure elongates the current path and reduces the current flow from port-1 to port-2, which enhances the isolation.

To analyze the CP behavior of the MIMO antenna, the simulated surface current is illustrated in Fig. 2d for 0^0, 90^0, $180^{0,}$ and 270^0 phases when port-1 is excited at 6 GHz frequency. The directions of the surface vector current are clock and anti-clockwise on both sides of the microstrip feed. This concludes that the antenna exhibits the property of RHCP and LHCP polarization and can receive the signal from any direction, irrespective of antenna placement.

4. ANTENNA PERFORMANCE WITH HUMAN-BODY INTERACTION

The proposed two-port antenna with improved isolation and exhibits circular behavior in the ISM band can be used in wearable devices. The SAR is analyzed of the proposed antenna with a simulated phantom model to validate the antenna for wearable application. SAR can be expressed with the help of the equation demonstrated in reference [19]. The SAR value must be under a predefined limit when the antenna is utilized for wearable applications, where the threshold is 1.6 W/kg, averaging 1g of tissue.

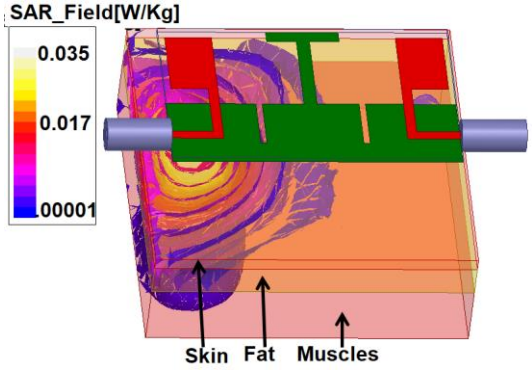

(a)

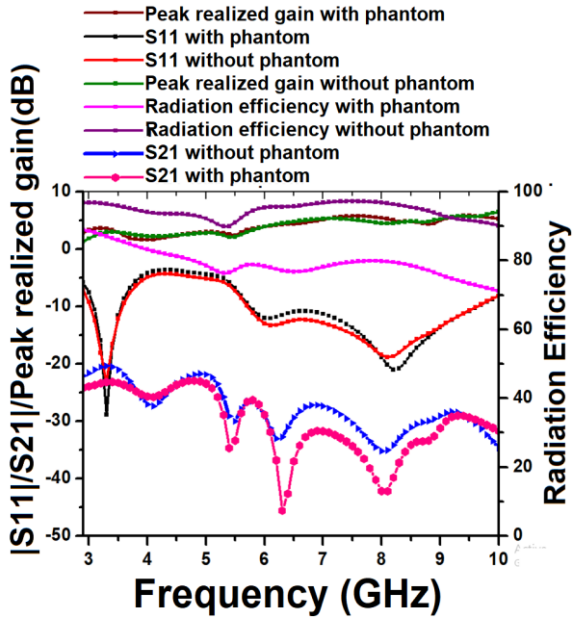

(b)

Fig. 3 – Phantom analysis: a) average simulated SAR of wrist model; b) $|S_{11}|$ /$|S_{21}|$ /Peak realized gain (dBi) /Radiation efficiency with and without phantom.

The phantom model consists of three layers: skin (2 mm), fat (5 mm), and muscles (10 mm), with the dimension of 50×50 mm^2. SAR is evaluated at a 5.8 GHz frequency for the proposed antenna at a 10 mm distance from the phantom model, as demonstrated in Fig. 3a. The electrical properties of tissue [20] at 5.8 GHz are illustrated as follows: skin (ε_r = 3.717 F/m, σ = 35.114 S/m, ρ = 1109 kg/m^3), fat (ε_r = 0.29313, σ = 4.9549 S/m, ρ = 911 kg/m^3) and muscles (ε_r = 4.9615, σ =48.485 S/m, ρ = 1090 kg/m^3). The maximum average and local SAR for 10 mW input power is 0.03 W/kg and 0.02 W/kg, respectively, which is far below the acceptable limit. The effect of the phantom model on antenna performance is evaluated in terms of S-parameter, radiation efficiency, and peak realized gain, as depicted in Fig. 3b.

5. SAR ANALYSIS FOR FEMALE BREAST TUMOR DETECTION

The proposed antenna represents the circular behavior in the ISM band (5.8 GHz) as it can be used for biomedical applications therefore, the simulation of the female breast phantom model is analyzed for early tumor detection where SAR is calculated. A female breast phantom is considered with three segments, namely skin, fat, and glandular tissue, as depicted in Fig. 4a. The electrical properties and thickness of the heterogeneous phantom are considered according to references [19, 20] and mentioned in Table 1 at the frequency of 5.8 GHz. A tumor is embedded in the glandular tissue at 37 mm from the proposed antenna with relative permittivity 50, conductivity of 4 S/m, and radius of 8 mm. To visualize cancerous tissue in female breast prototypes, the average and local value of SAR for breast phantom at 1 W power is simulated, averaging over 1 g of tissue. The simulated SAR with and without tumor cells is also depicted in Fig. 4b – c.

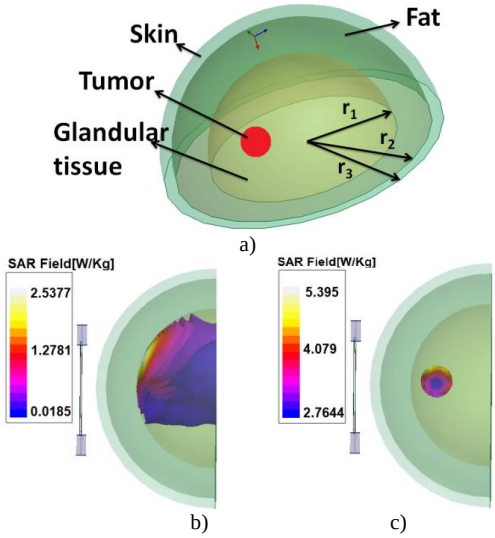

Fig. 4 – a) Female breast model breast at 5.8 GHz; b)SAR of glandular tissue with tumor; c) SAR of tumor in glandular tissue.

Table 1

Electrical Properties of human female

Human Tissue	Skin	Breast fat	Glandular tissue
Relative permittivity	36.18	4.9549	12
Conductivity (S/m)	3.717	.29313	.5
Mass density (kg/m^3)	1109	911	1090

The maximum average SAR with tumor is 10.78 W/kg (skin), 18.72 W/kg (fat), 2.53 W/kg (glandular tissue), and 5.39 W/kg (tumor). The maximum average SAR without tumor is 11.10 W/kg (skin), 18.84 W/kg (fat), and 2.43 W/kg (glandular tissue). The maximum local SAR with a tumor is 15.71 W/kg (skin), 31.12 W/kg (fat), and 3.90 W/kg (glandular tissue), while the top local SAR without a tumor is 16.92 W/kg (skin), 33.18 W/kg (fat), and 3.67 W/kg (glandular tissue). Two significant findings have emerged in breast cancer detection by above mentioned SAR investigation.

- The first finding signifies that the SAR value with and without tumor tissue in the phantom model differs.
- The second finding represents that the SAR value of tumor tissue is more significant than its surrounding glandular tissue.
- These two findings can be utilized in tumor detection applications in the female breast.

6. RESULTS AND DISCUSSIONS

In this section, the prototype antenna is fabricated, and S-parameter is measured using the vector analyzer Anritsu MS2038C. The experimental and simulated values of $|S_{11}|$ and $|S_{21}|$ are compared to justify the dual-band antenna design, as illustrated in Fig. 5a. Both responses are similar except for a slight discrepancy due to losses in the SMA connector, manufacturing error, and parasitic effect in soldering. The designed antenna displays the dual-band characteristic from 3 GHz to 3.6 GHz (5G for smartphone applications) and 5.7 GHz to 9.7 GHz (for special UWB applications) that resonates at 3.3 GHz 8.1 GHz, respectively. The minimum isolation for the first band is 20.4 dB and for the second band is 26.5 dB. The measured value of the axial ratio is shown in Fig. 5b. An anechoic chamber is utilized to measure the normalized co-polar and cross-polar radiation pattern in the two principal planes *YZ* and *ZX* at the resonance frequency 3.3 GHz and 6 GHz (RHCP and LHCP), as depicted in Fig. 5c, when port-1 is excited, and port-2 is terminated by 50 Ω load. A comparatively stable 2D radiation pattern is observed at the lower resonance frequency and higher frequency. The peak realized gain at the lower and higher resonance frequency is 3 dBi and 5 dBi, respectively, as shown in Fig. 5d. The radiation efficiency is above 90% in both operating bands, as shown in Fig. 5e.

The diversity estimation of the multi-input multi-output antenna is performed by the envelope correlation coefficient, as shown in Fig. 5f. For good diversity performance and practical applications, the ECC should be less than 0.5 in the operating bandwidth, which can be calculated using equation (2) [21]. TARC and Directive gain (DG) is COMPUTED from eq. (3) and (4) where DG is closed to 10 dB, and minimum variation is achieved on TARC in different phases [21]. CCL is another parameter that defines the diversity characteristic of the MIMO antenna. The channel capacity of the MIMO antenna is directly related to the number of antenna elements. The channel capacity loss is an important factor in defining MIMO performance, and its value should be less than 0.4 bits/sec/Hz. The CCL can be expressed as equation (5) in terms of scattering parameters where its calculated value is less than the acceptable limit [17].

Table 2

Comparison between previous published paper in literature

Ref.	**Size (mm)**	**Band (GHz)**	**Isolation (dB)**	**Technique used**
[2]	55×80×1.6 55×100×1.6	2.45/5.25 1.8/3.5	< 15	Transmission line decoupling network
[3]	65×61×.8	1.56-2.71 4.82-5.9	–15 –15	DGS with meandered lines
[4]	60×60×1.6	2.4-2.48 5.15-5.825	–25 < –20	Meandering line resonator & parasitic elements
[5]	38×18.2×0.762	2.3-2.5 5-5.2	–20 –20	Metal strips with shorting vias
[6]	43×26×.8	2.34-2.47 3.35-3.64	–32 –18	Metamaterial s
[7]	30×26×1.6	3.2-3.8 5.7-6.2	–20 –20	Elliptical slot & parasitic strip
[8]	72×56×.8	2.24-2.90 3.9-7.55	< –24	Metal strips
[9]	35×69.5×1.5	3.37-3.4 4.94-4.98	–17 –23	WG-MTM
[10]	52×77.5×1.6	2.4-2.48 5.15-5.828	–-15	Meandering line resonator & slot
[11]	85×120×1.6	2.4-2.5 5.75-5.85	18 –22	T-stub circuits
Proposed antenna	28×45×8	3-3.6 5.7-9.7	–20.4 –26.5	T-stub & slots

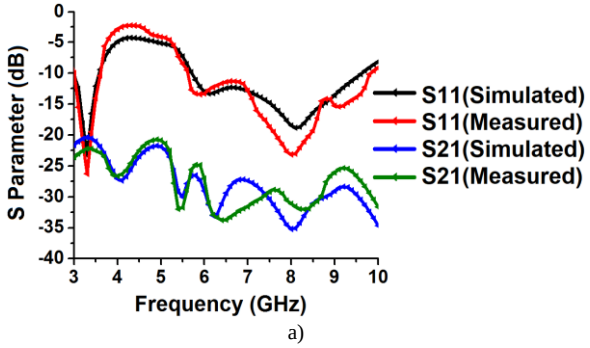

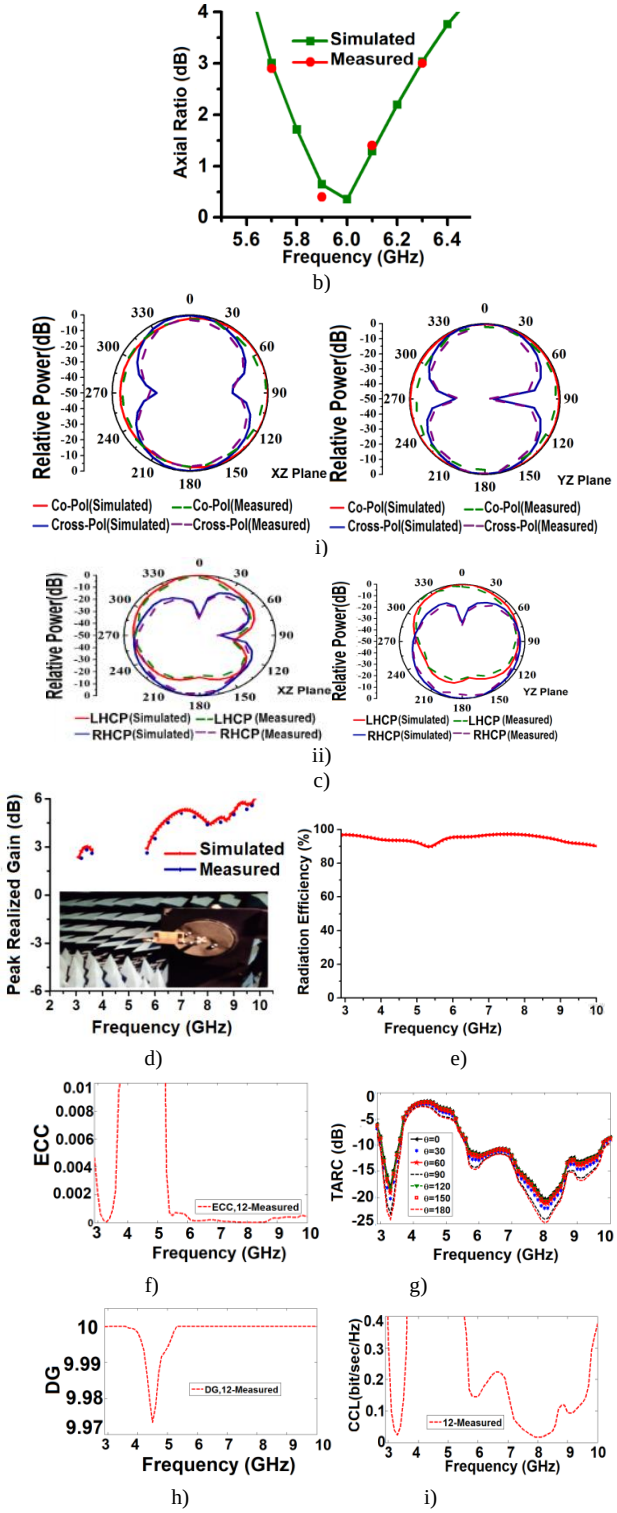

Fig. 5 – a) *S* – parameter (measured and simulated); b) axial ratio; c) CoPol. and Cross-Pol. radiation pattern at (i) 3.3 GHz in the upper row and (ii) 6 GHz (RHCP and LHCP) in the lower row; d) peak realized gain; e) radiation efficiency; f) ECC; g) TARC, h) DG (i) CCL.

$$\mathrm{ECC}=\frac{\left|S^{*}_{11}S_{12}++S^{*}_{21}S_{22}\right|^{2}}{\left(1-\left|S_{11}\right|^{2}-\left|S_{21}\right|^{2}\right)\left(1-\left|S_{22}\right|^{2}-\left|S_{12}\right|^{2}\right)} \quad (2)$$

$$\mathrm{TARC}=\sqrt{\left|S_{11}+S_{12}e^{j\theta}\right|^{2}+\left|S_{22}e^{j\theta}+S_{21}\right|^{2}}/\sqrt{2} \quad (3)$$

$$\mathrm{DG}=10\sqrt{1-\left|\mathrm{ECC}\right|^{2}} \quad (4)$$

$$\mathrm{CCL}=-\log_{2}\det\left(\psi^{R}\right). \quad (5)$$

The proposed CP-MIMO antenna is compared with previously published literature [4–13] in terms of size, bandwidth, isolation, fabrication material, techniques used, peak realized gain, ECC, CCL, and efficiency are presented in Table 2.

The work presented in the literature is used to design a MIMO antenna with comparatively low isolation. The proposed antenna is compact in size, has high isolation with defective ground structure, and has accessible decoupling technology.

7. **CONCLUSIONS**

This paper proposed and demonstrated the compact and circular polarized dual-band MIMO antenna with a simple decoupling structure for 5G mobile communication, wearable, and tumor detection applications. CP-MIMO antenna contributes dual-band (3 GHz–3.6 GHz, 5.7 GHz–9.7 GHz) and axial ratio bandwidth of 5.7 GHz–6.3 GHz in the second band. Open-ended slots and T-shaped decoupling structure is responsible for isolation (> 20.4 dB in the first band and > 26.5 dB in the second band). The open slots also introduce the CP behavior by regulating the surface current in the ground plane. SAR is also simulated at 1 g of human tissue, which investigates and reveals that the proposed antenna is a good choice for wearable and cancer detection applications.

Received on 21 December 2021.

REFERENCES

1. B. Bag, P.P. Sarkar, *Dual-band monopole antenna for WLAN/WIMAX applications*, Rev. Roum. Sci. Techn. – Électrotechn. et Énerg., **63**, *3*, pp. 283–288 (2018).
2. N.K. Kiem, D.N. Chien, *A transmission line decoupling technique for enhancement of port isolation of dual-band MIMO antennas*, J. of Electromagnetic Waves and Applications, **32**, *10*, pp. 1195–1211 (2018).
3. Q. Li, M. Abdullah, X. Chen, *Defected ground structure loaded with meandered lines for decoupling of dual-band antenna*, Journal of Electromagnetic Waves and Applications, **33**, *13*, pp. 1764–1775 (2019).
4. J.Y. Deng, Z.J. Wang, J.Y. Li, L.X. Guo, *A dual-band MIMO antenna decoupled by a meandering line resonator for WLAN applications*, Microwave and Optical Technology Letters, **60**, *3*, pp. 759–765 (2018).
5. D. Sipal, M. P. Abegaonkar, S.K. Koul, *Highly isolated compact planar dual-band antenna with polarization/pattern diversity characteristics for MIMO terminals*, IEEE Antennas and Wireless Propagation Letters, **18,** *4*, pp. 762–766 (2019).
6. A.K. Panda, S. Sahu, R. K. Mishra, *A compact dual-band 2×1 metamaterial inspired MIMO antenna system with high port isolation for LTE and WiMax applications*, International Journal of RF and Microwave Computer-Aided Engineering, **27**, *8*, pp. e21122 (2017).
7. P.C. Nirmal, A. Nandgaonkar, S.L. Nalbalwar, R.K. Gupta, *A compact dual band MIMO antenna with improved isolation for Wi-Max and WLAN applications*, Progress in Electromagnetics Research M, **68**, pp. 69–77 (2018).
8. A. Kumar, A.Q. Ansari, B.K. Kanaujia, J. Kishor, *A novel ITI-shaped isolation structure placed between two-port CPW-fed dual-band MIMO antenna for high isolation*, AEU-International Journal of Electronics and Communications, **104**, pp. 35–43 (2019).
9. C. Guo, H. Zhai, S. Liu, *A new dual-band microstrip antenna array with high isolation by waveguided metamaterial structure*, Microwave and Optical Technology Letters, **61**, *5*, pp. 1365–1370 (2019).
10. S. Chouhan, D.K. Panda, V.S. Kushwah, S. Singhal, *Spider-shaped fractal MIMO antenna for WLAN/WiMAX/Wi-Fi/Bluetooth/C-band applications*, AEU-International Journal of Electronics and Communications, **110**, pp. 152871 (2019).
11. J. Deng, J. Li, L. Zhao, L. Guo, *A dual-band inverted-F MIMO antenna with enhanced isolation for WLAN applications*, IEEE Antennas and Wireless Propagation Letters, **16**, pp. 2270–2273 (2017).

12. J. Sui, K.L. Wu, *A general T-stub circuit for decoupling of two dual-band antennas*, IEEE Transactions on Microwave Theory and Techniques, **65**, *6*, pp. 2111–2121 (2017).
13. F.A. Dicandia, S. Genovesi, A. Monorchio, *Analysis of the performance enhancement of MIMO systems employing circular polarization*, IEEE Transactions on Antennas and Propagation, **65**, *9*, pp. 4824–4835 (2017).
14. I.C. Stanica, F. Moldoveanu, M.I. Dascalu, I.V. Nemoianu, G.P. Portelli, *Advantages of telemedicine in neurorehabilitation and quality of life improvement*, Rev. Roum. Sci. Techn. – Électrotechn. et Énerg., **66**, *3*, pp. 195–199 (2021).
15. H. Gupta, P. Kumar, S. Saurabh, S. K.Mishra, B. Appasani, A. Pati, A. Srinivasulu, *Category boosting machine learning algorithm for breast cancer prediction*, Rev. Roum. Sci. Techn. – Électrotechn. et Énerg., **66**, *3*, pp. 201–206 (2021).
16. S.P. Biswal, S. Das, *Eight-element-based MIMO antenna with CP behaviour for modern wireless communication*, IET Microwaves, Antennas & Propagation, **14**, *1*, pp. 45–52 (2020).
17. A. Kumar, A. De, R.K. Jain, *Circularly polarized CPW fed MIMO/Diversity antenna for Wi-Fi and WLAN applications*, Frequenz, **76**, *1-2*, pp. 37–44 (2022).
18. R. Chandel, A.K. Gautam, K. Rambabu, *Tapered fed compact UWB MIMO-diversity antenna with dual band-notched characteristics*, IEEE Transactions on Antennas and Propagation, **66**, *4*, pp. 1677–1684 (2018).
19. S. Subramanian, B. Sundarambal, D. Nirmal, *Investigation on simulation-based specific absorption rate in ultra-wideband antenna for breast cancer detection*, IEEE Sensors Journal, **18**, *24*, pp. 10002–10009 (2018).
20. http://niremf.ifac.cnr.it/tissprop/htmlclie/htmlclie. php
21. A. Kumar, *Compact 4×4 CPW-Fed MIMO antenna with Wi-Fi and WLAN notch for UWB applications*, Radioelectronics and Communications Systems, **64**, *2*, pp. 92–98 (2021).
22. A. Kumar, A. De, R.K. Jain, *CSRR and open-stub based circular polarized and double band eight-ports MIMO antenna for 5G and ISM band applications*, Microsystem Technologies, **28**, pp. 1727–1738 (2022).